Peroxidase-mimicking evodiamine/indocyanine green nanoliposomes for multimodal imaging-guided theranostics for oral squamous cell carcinoma

Zheng Wei [a,c,e,1], Huihui Zou [a,e,1], Gongyuan Liu [g], Chuanhui Song [a,e], Chuanchao Tang [a,e], Sheng Chen [f], Guorong Zhang [d], Jianchuan Ran [a,e], Yufeng Wang [a,e], Xiteng Yin [a,e], Yu Cai [b,e,**], Wei Han [a,e,*]

[a] *Department of Oral and Maxillofacial Surgery, Nanjing Stomatological Hospital, Medical School of Nanjing University, 30 Zhongyang Road, 210008, Nanjing, China*
[b] *Clinical Research Institute, Zhejiang Provincial People's Hospital, People's Hospital of Hangzhou Medical College, No. 158 Shangtang Road, Hangzhou, 310014, Zhejiang Province, China*
[c] *Pediatric Dentistry, Nanjing Stomatology Hospital, Medical School of Nanjing University, No 30 Zhongyang Road, Nanjing, 210008, China*
[d] *Department of Orthodontics, Nanjing Stomatological Hospital, Medical School of Nanjing University, No 30 Zhongyang Road, Nanjing, 210008, China*
[e] *Central Laboratory of Stomatology, Nanjing Stomatological Hospital, Medical School of Nanjing University, 30 Zhongyang Road, 210008, Nanjing, China*
[f] *Department of Oral Pathology, Nanjing Stomatological Hospital, Medical School of Nanjing University, Nanjing, China*
[g] *Department of Chemistry, City University of Hong Kong, 83 Tat Chee Avenue, Hong Kong SAR, China*

ARTICLE INFO

ABSTRACT

Here, evodiamine (EVO) and the photosensitizer indocyanine green (ICG) were integrated into a liposomal nanoplatform for noninvasive diagnostic imaging and combinatorial therapy against oral squamous cell carcinoma (OSCC). EVO, as an active component extracted from traditional Chinese medicine, not only functioned as an antitumor chemotherapeutic agent but was also capable of ^{68}Ga-chelation, thus working as a contrast agent for positron emission tomography/computed tomography (PET/CT) imaging. Moreover, EVO could exhibit peroxidase-like catalytic activity, converting endogenous tumor H_2O_2 into cytotoxic reactive oxygen species (ROS), enabling Chemo catalytic therapy beyond the well-known chemotherapy effect of EVO. As proven by *in vitro* and *in vivo* experiments, guided by optical imaging and PET/CT imaging, we show that the theragnostic liposomes have a significant inhibiting effect on in situ tongue tumor through photodynamic therapy combined with chemodynamic chemotherapy.

1. Introduction

Cancer is projected supposed to rank as the leading cause of death and the most significant barrier for increasing life expectancy globally in the 21st century. Lip and oral cavity cancers, with 50 thousand incident cases in 2018, were the top 15 most common cancers worldwide [1].

Oral squamous cell carcinoma (OSCC) is a lethal and deforming disease with rising incidence; it painfully hampers the chewing and swallowing capability and leads to a devastating disfiguring of patients [2]. Although the management of OSCC has significantly been ameliorated, only a minor improvement of OSCC survival has been obtained over the past 30 years, partly because of the difficulty in obtaining 'clear' cancer

---

surgical margins and effective chemical drugs or radiation therapies [3]. OSCC patients' postoperative living quality is closely related to surgical margins. The postoperative survival rate of the OSCC patients who had dysplastic margins showed significantly better than those with positive margins. And the local recurrence ratio is also considerably increased with positive margins [4–6].

Therefore, noninvasive and accurate diagnostics of OSCC lesions integrated with high mortality and significant toxicity-advanced therapy modalities are urgently needed [5,6]. Near-infrared (NIR) fluorescence imaging and phototherapy thus drew our attention for their potent antitumor efficacy, noninvasiveness imaging, and controlled normal tissue damage [7–10], and some exciting results from preclinic experiments of NIR fluorescence imaging have been reported [11–14]. Photodynamic therapy (PDT), which generates toxic ROS with the assistance of a photosensitizer under laser irradiation, exhibited great potential against OSCCs in recent studies [15,16]. Ren et al. prepared PEG-PCL-C_3-ICG to treat OSCC using the HSC3 cell line showing significant PDT efficacy [17]. Besides, the Eka-Putra Gusti-Ngurah-Putu team reported that PDT + lipid-platinum-chloride nanoparticles significantly reduced tumor volume by up to ~112% on the OSCC xenograft model [18]. Yet, single-modal PDT's therapeutic effect was compromised mainly because of the tumor microenvironment-related hypoxia or certain anti-oxidant defense mechanisms [19]. Therefore, strategies should be considered to overcome the hypoxia-related PDT failure.

To defeat the TME-related resistance of PDT, combinatorial therapeutic modalities were integrated for OSCC treatment, such as chemotherapy [20]. Recently, traditional Chinese medicine extraction components were shown to have great potential in antitumor applications and have been recognized as a fertile source for revealing novel lead molecules for drug discovery. For instance, Zhou's team found that Icaritin could reduce OSCC progression via the inhibition of STAT3 signaling [21]. And TBMS1 was reported to significantly suppress proliferation as well as migration on OSCC cells [22]. Evodiamine (EVO) is an alkaloid extracted from the fruit of *Evodia rutaecarpa Benth*am. In southeast countries (China, Korea, and Japan) [23], EVO has been used to treat several chronic diseases in clinic practices of traditional Chinese Medicine, for instance, abdominal pain, headaches, vomiting, colds, and reduced blood circulation. And Fructus evodiae mixed with ginger juice took effect for diabetic gastroparesis in a clinical study [24]. Studies also showed that EVO would be a potential therapeutic drug against other diseases such as hypomotility disorders [25], renal tubulointerstitial fibrosis [26], and IgE-induced allergenic diseases (including rhinitis and atopic dermatitis) [27]. Recently, EVO was widely reported to have the potential to become a therapeutic medicine for treating various cancers [28,29] due to its ability to cause tumor cell apoptosis by suppressing the NF-κB activity on tongue cancers both *in vitro* and *in vivo* [30]. A famous pill called *Zuojin* Pills, containing EVO, could be used for hepatocellular carcinoma treatment [31]. However, its clinic application was greatly hampered by its hydrophobicity, low oral bioavailability, short half-life period, and poor understanding of antitumor mechanisms and potential side effects on hepatic cells and cardiac cells [32]. To solve the hydrophobicity, Wang et al. developed GE11-Evo-NPs that were confirmed soluble and better retained cancer cell cytotoxicity than free EVO [33]. To track the distribution of EVO inside cells, a novel fluorescent probe named 10-hydroxyevodiamine was prepared, and it was observed in mitochondria and lysosomes [34]. Yet, these studies did not involve OSCC, and the exploitation of EVO was not sufficient. Therefore, designing a nano delivery system loading EVO should be an efficient way to surmount those limitations, observe the effect of treating OSCC, and closely monitored its potential side effect of hepatotoxicity and cardiotoxicity [35,36].

Beyond the integration of chemotherapy, another therapeutic method is to use and disturb TME by enzymatic catalysis or Fenton-like reactions since the upregulated amount of H_2O_2 is one of the significant characteristics of TME, catalase or catalase-mimic agents that are capable of generating oxygen from H_2O_2, thus relieving tumor hypoxia and promoting the efficacy of PDT [37]. At the same time, horseradish peroxidase (HRP)-mimic or Fenton-like agents can generate ROS directly via catalytic or metal-assisted redox reactions, which is called Chemodynamic therapy (CDT) [38–40]. Such TME targeted antitumor approaches not only directly kill tumor cells with ROS but also shake the fundamental prerequisites for tumor growth and metastasis by hampering TME.

Here, for integrated diagnostic imaging and combinatorial therapy, EVO and ICG, a Food and Drug Administration (FDA) of the US approved NIR photosensitizer, were encapsulated into a theragnostic nanoliposome system (namely EI@Lipo). Owing to the liposomal vehicle, the intrinsic poor water solubility of EVO was significantly improved, and the tumor passive targeting ability based on enhanced permeability and retention (EPR) effect was also achieved. With the presence of EVO and ICG, EI@Lipo presented both the chemo-antitumor effect and PDT effect on OSCC. Furthermore, EVO was found to be capable of HRP-like catalysis, which converted endogenous tumor H_2O_2 into ROS, as an auxiliary CDT antitumor modality. Using orthotropic mice, OSCC model-based experiments, *in vivo* optical imaging was accomplished by ICG, and PET/CT imaging was conducted through ^{68}Ga labeled EVO, which enabled the early detection of systemic tumor and effective evaluation of tumor metabolism. Guided by optical imaging and PET/CT imaging, EI@Lipo showed outstanding tumor inhibition via tri-modal combinatorial chemo/chemodynamic/photodynamic combinatorial therapy. These results also provided insights into the anticancer mechanism of EVO, and the potential future drug development for OSCC treatment.

2. Materials and methods

2.1. Synthesis of liposome

EI@Lipo encapsulating EVO and ICG was fabricated by using a typical thin-film spin evaporation process. Briefly, phosphatidylcholine (5 mg), chole (3 mg), ICG (1 mg), and DSPE-mPEG$_{2000}$ (1 mg) were dissolved in 1–2 mL of methanol. Then, EVO (1 mg) was dissolved in chloroform (1 mL). The mixed organic solvent was evaporated by rotary evaporation, and then films were formed layer by layer. Subsequently, the films were dissolved in 2 mL of deionized water (DI water) or polarization beam splitter (PBS) through sonication at room temperature for 20 min until a clear dispersion of EI@Lipo was obtained. EVO@Lipo, ICG@Lipo, and Lipo vehicle were synthesized following the same process.

3. Characterization of every type of liposomes

UV–Vis–NIR spectrophotometer (Shimadzu UV-2550, Japan) was used to determine the UV–Vis–NIR absorption spectra of the EI@Lipo, EVO@Lipo, and ICG@Lipo. The fluorescence spectrometer was conducted to test the fluorescence spectrum of EI@Lipo, EVO@Lipo, and ICG@Lipo. Liposomes and EI@Lipo were measured by a transmission electron microscope (TEM, Hitachi H-7600, Japan) to analyze the structure and morphology. The diameter of the EI@Lipo were tested by dynamic light scattering (DLS). To detect the stability of EI@Lipo, the UV–Vis–NIR absorption spectra, DLS and TEM of EI@Lipo were conducted at the 0-day, 7th day and 14th day after the EI@Lipo in PBS (pH = 7.4) was synthesized.

4. Drug embedding rate and release

EVO and ICG were dissolved with tetrahydrofuran (THF) with the concentration of 1000 μg/mL and 500 μg/mL, 250 μg/mL, 125 μg/mL and 62.5 μg/mL, respectively. The UV–Vis–NIR absorption spectra were measured and the linear fitting solubility curves were made. Part of the EI@Lipo were lyophilized, and then the lyophilized products were dissolved with THF, and their UV absorption spectra were measured.

According to linear fitting solubility curves, the total amount of EVO and ICG in freeze-drying products was calculated, and finally the drug encapsulation efficiency of EVO and ICG was calculated. The pH-responsive drug release behavior was conducted via UV–vis–NIR spectrophotometer. EVO and ICG released from the EI@Lipo were detected at pH 7.40, pH 7.06, pH 6.00, pH 4.60 as follows: 2 mL of EI@Lipo was transfused into a dialysis bag (molecular weight: 1000 Da). Then the dialysis bag was immersed into 200 mL of different pH PBS with magnetic stirring at the speed of 1200 rpm. At each time point, the outer dialysate was collected and replaced with fresh PBS. The drug release experiment was observed for 72 h. The PDT effect of EI@Lipo and ICG@Lipo.

The PDT effect of EI@Lipo and ICG@Lipo was measured by ROS generation through singlet oxygen sensor green (SOSG). Each detection process was followed by each standard rule of the corresponding instrument. SOSG powder was dissolved in methanol to make a 500 μM stock solution. The work concentration of SOSG was 5–50 μM. Test samples and SOSG reagents were in aqueous solution. NIR laser (808 nm, 100 mW/cm², 1 min) was used as a light source to excite ICG. The experiment was performed three times, and emission at ~525 nm was recorded.

To compare the singlet oxygen quantum yield of EI@Lipo and free ICG, the same method was adopted with SOSG. The singlet oxygen quantum yield of ICG was 0.077 ($\Phi = 0.077$) [41]. The singlet oxygen quantum yield of EI@Lipo was calculated with the formula as follow:

$$\Phi_T = \Phi_{ICG}\left(\frac{S_T}{S_{ICG}}\right)\left(\frac{F_{ICG}}{F_T}\right)$$

$$F = 1 - 10^{-OD}$$

Φ represents singlet oxygen yield; S is the slope of a linear fitting line with the irradiation time as X axis and the fluorescence intensity of SOSG at 525 nm as Y axis; F represents the absorption correction factor of the test and reference materials. The OD value is the UV–Vis absorption of test and reference materials at 808 nm [42].

5. HRP-like catalysis of EVO to generate ROS

To clarify how EVO could enhance ROS production, H_2O_2 catalysis and HRP assays were conducted using Catalase Activity (CAT)Assay Kit and HRP kit, respectively. To each well of a 96-well plate, 100 μL of diluted assay buffer, 30 μL methanol, and 20 μL of EVO, EVO@Lipo, or EI@Lipo solutions were added. Each type of sample was tested in triplicate. 20 μL of diluted hydrogen peroxide was then added to all each of the tested wells, followed by 10 μL of catalase potassium periodate to each well for a 20-min incubation at room temperature. The absorbance was read at 540 nm using a plate reader. The experiments were repeated three times. Then, 3,3′,5,5′-tetramethylbenzidine (TMB) was used for HRP color-reaction. TMB can act as a hydrogen donor for H_2O_2 reduction by peroxidase enzymes such as HRP. A blue reaction product is formed that can be read at the wavelengths of 370 nm and 650 nm. EVO@Lipo and overdose H_2O_2 were mixed for 0, 1, 5, 10, and 15 min, and an overdose of TMB was added to the reaction system. Finally, the blue production was read at 370 nm and 650 nm using a UV–Vis–NIR spectrophotometer.

6. Cell culture

The OSCC cell line CAL27 and oropharyngeal carcinoma cell line Fadu were purchased from the American Type Culture Collection (ATCC; Manassas, VA, USA). CAL27 and Fadu cells were cultured in high-glucose Dulbecco's modified Eagle's medium (DMEM) with 10% (v/v) fetal bovine serum and 1% (v/v) 100 U/L penicillin, and 100 μg/mL streptomycin. The cells were cultured in an incubator at 37 °C with 5% CO_2.

7. Cellular uptake

Approximately CAL27 cells and Fadu (1×10^4) were cultured overnight in a confocal dish. Then, the medium was changed with a conditioned medium containing EVO, EVO@Lipo, or EI@Lipo and cultured for 24 h. After discarding the supernatant, the cells were fixed with glutaraldehyde. LysoTracker Green DND-26, ER-Tracker Green and MitoTracker Deep Red FM (Nanjing warbio Biotechnology Co., Ltd) were used for colocation in cells with green, yellow and red fluorescence. Method was followed the product instructions. Untreated control and treated cells were observed under a confocal microscope (NIKON Ti, Japan). The colocalization of EVO with lysosome, Endoplasmic reticulum and mitochondria was analyzed by ImageJ software with Pearson's correlation coefficient.

8. Cellular ROS detection

A Reactive Oxygen Species Assay Kit (Beyotime Biotechnology, China. S0033S) was used to detect the ROS generation in cells. CAL27 cells were cultured with the conditioned medium of the three groups (Control, ICG@Lipo, and EI@Lipo) for 6 h. Following the instructions of the assay kit, we then treated cells with an 808 nm laser (100 mW/cm²) for 10 min. Finally, the samples were immediately analyzed the ROS production by a confocal microscope. All operations were in the dark, and the experiments were repeated three times.

9. Cytotoxicity assay

The viability of CAL27 and Fadu cells was evaluated using the CCK-8 kit (Bimake, Houston TX, USA). CAL27 and Fadu cells were seeded in 96-well plates at a density of $4 - 6 \times 10^3$ cells per well. The cells were incubated for 6 h with various concentrations of EVO, EVO@Lipo, ICG@Lipo, and EI@Lipo from 0 μg/mL to 50 μg/mL. The concentration was calculated by the drug embedding ratio. After incubation for 24 h, 10 μL of CCK-8 was added to each well, followed by incubation for 1–2 h at 37 °C. Finally, SpectraMax M3 was used to calculated cell viability at 450 nm.

10. Cell colony formation assay

CAL27 and Fadu single-cell suspensions were seeded into 6-well plates with 2000 cells per well. The concentration of drug components was 10 μg/mL. A single cell could grow into a colony over a 2-week culture. After discarding the supernatant, the colonies were fixed with glutaraldehyde (6.0% v/v), stained with crystal violet (0.5% w/v), and counted using a microscope. In this assay, only lives cells could be stained and counted. Finally, results were analyzed by ImageJ software.

11. Wounding healing assay

The CAL27 cells were seeded in a six-well plate and grown to confluency. Then, a 10-μL pipette tip was used to press perpendicularly on the cells layer and draw a straight line to create a scratch model. Next, the wound was imaged every 6 h. In addition, 3–5 points were picked randomly, and cell migration was measured by calculating the distance between two edges in the wound area over time. Finally, results were analyzed by ImageJ software.

12. In vitro chemodynamic therapy evaluation

The chemodynamic therapy effect *in vitro* on live and dead cells was measured in two ways with the staining kit and apoptosis detection kit, respectively. CAL27 cells were seeded in six-well plates and incubated overnight. The medium was replaced with fresh DMEM containing blank, EVO, EVO@Lipo, ICG@Lipo (two grows), EI@Lipo (two grows). After incubation for 12 h, cells in the ICG@Lipo and EI@Lipo groups
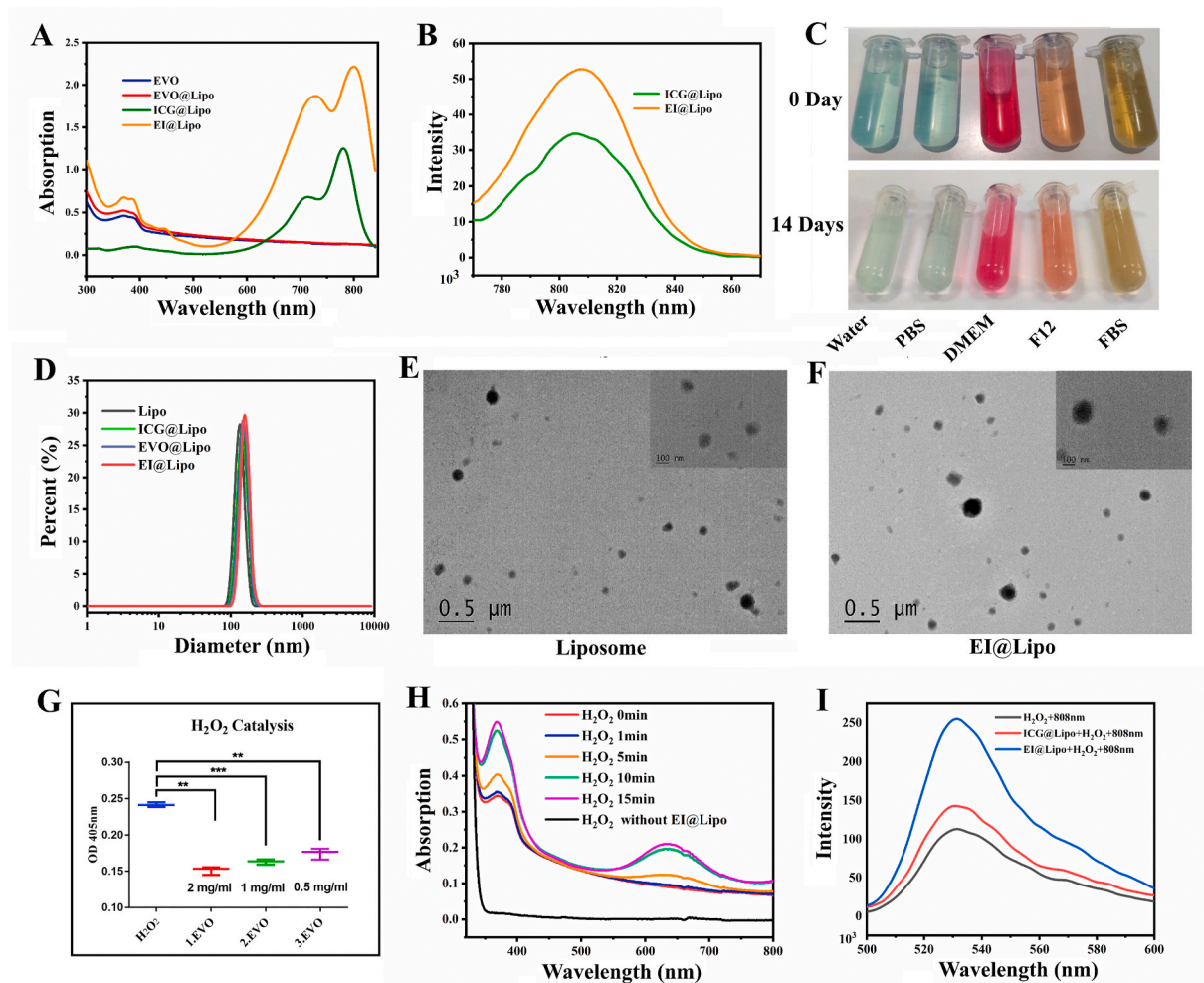
Fig. 1. The characteristics of EI@Lipo and the basic components. A. The UV absorption of EVO, EVO@Lipo, ICG@Lipo, and EI@Lipo in blue, red, green, and orange lines, respectively. **B.** The fluorescence of ICG@Lipo (green) and EI@Lipo (orange). **C.** EI@Lipo was stored in various solutions for two weeks, namely water, PBS, DMEM, F12, and FBS. **D.** DLS detection of nano Liposomes, ICG@Lipo, EVO@Lipo, and EI@Lipo. **E** and **F.** The average diameter of various nanoliposomes ranged from 110 nm to 120 nm. The TEM result of Liposomes and EI@Lipo. In addition, the average diameters of Liposomes and EI@Lipo were approximately 110 nm and 120 nm, respectively, which was consistent with the DLS result. In addition, the size of EI@Lipo was a little bit larger than free Liposomes. Scale bar = 0.5 μm (big). Scale bar = 100 nm (small). **G.** EVO could decompose H_2O_2, and this capability was EVO-concentration dependently. $**p < 0.01$, $***p < 0.001$. **H.** TMB could be oxidized in the presence of EVO and H_2O_2, and the product's UV-VIS absorption peak occurred at 370 nm and 625 nm. In addition, the result showed that EVO had horseradish peroxidase-like properties. **I.** Singlet oxygen production could be significantly enhanced in the EI@Lipo + H_2O_2 group.

were exposed to 808 nm laser (100 mW/cm²) for 5 min. Next, the cells were labeled using a different kit. First, the cells were washed three times with PBS and treated with Calcein-AM/PI Double Staining Kit to label live cells in green and dead cells in red under the confocal microscope. Besides, the cells were treated using an Annexin V-FITC/PI Apoptosis Detection Kit (Vazyme Biotech Co., Ltd, China) to label early-period dead cells in green and late-period cells in red by flow cytometer. All procedures were conducted according to the manufacturer's instructions.

13. Solid tumor model construction *in vitro*

Solid tumor models were generated by spheroid aggregation of CAL27 cells and growth in suspension. First, 2000–4000 cells were seeded in non-adherent surfaced six-well plates. Cells were then carefully cultured without too much movement in serum-free DMEM/F12 medium containing 10 ng/mL basic fibroblast growth factor, 20 ng/mL epidermal growth factor, and 2% B-27 supplement (v/v) and 1% streptomycin, and penicillin (v/v) in an incubator at 37 °C with 5% CO₂ for two weeks. Sphere formation was assessed by a microscope. EI@Lipo penetration and PDT effect examination on the solid tumor model.

Upon the solid tumor model formation, EVO and EI@Lipo (concentration of EVO was 30 μg/mL) were added to the different media to assess the penetration of the nanoliposomes. After culturing for 24 h, the spheres were carefully sucked, washed with PBS, and placed on confocal dishes. Finally, the penetration effect was examined by an inverted laser confocal microscope (Zeiss LSM 880 with Airyscan). After EI@Lipo penetrated deeply in a solid tumor model, PDT was conducted with 100 mW/cm² 808 nm laser for 15 min.

14. In situ OSCC mouse model establishment

5 to 6 -week-old Balb/c male nude mice were purchased from Nanjing Biomedical Research Institute of Nanjing. CAL27 cells($3-5 \times 10^4$) were injected into the tongue of mice under anesthesia. All animal experiments were followed by the guidelines international and national approved by the Nanjing Stomatological Hospital Ethics Committee.

[68]Ga radiolabeling of nanoliposomes.

To ^{68}Ga-label in EI@Lipo, 2 mL nanoliposome solution and 2 mL of [68]GaCl₃ ([68]GaCl₃ was provided by the Department of Nuclear Medicine, Nanjing First Hospital, affiliated with Nanjing Medical University) were

mixed with 2–3 mL of dehydrated alcohol as a dispersing agent. These components were blended and heated in a boiling water bath for 20–30 min. After radiolabeling, a sample of each of the resulting products was analyzed by radio-HPLC [43]. The radiochemical purity was >90% for micro PET-CT imaging studies.

15. In vivo bioimaging

When the length of tongue cancer reached 4 mm, mice bearing in situ Squamous cell carcinoma tumors were imaged by micro PET-CT and fluorescence imaging instrument. Mice were injected with 100 μL of PBS, EVO, EVO@Lipo, ICG@Lipo, and EI@Lipo (corresponding to 2 mg/kg EVO and ICG) via the tail vein. Micro PET-CT imaging and fluorescence imaging under 808 nm laser were recorded every 0.5 h and 1 h, respectively.

16. Anticancer evaluation *in vivo*

Twenty-one CAL27 tongue cancer nude mice (n = 3) were injected with 100 μL of PBS or PBS containing different drugs at a dose of 2 mg/kg for EVO or ICG (free molecule). Thirty minutes after injection, the tongue tumors were exposed to 808 nm laser (1 mW/cm^2) for 10 min. Therapies were conducted every three days, and every mouse received five treatments. In addition, before therapies, the body weight and tumor size were measured. The tumor volume was calculated as "length × width × height". All operations were performed under anesthesia. Finally, tongue tumors were collected, measured, and stained by H&E and Ki-67. Furthermore, the heart, liver, spleen, lung, and kidney of every mouse were collected and stained by H&E.

17. Chronic toxicity experiment

Fifteen Sprague-Dawley (SD) rats (n = 3) were fed with water or water containing EVO, EVO@Lipo, ICG@Lipo, and EI@Lipo (corresponding to 2 mg/kg EVO and ICG) for 60 days. Blood was taken every five days for routine blood tests and liver and kidney function tests.

18. Statistical analyses

GraphPad Prism 7.0, Origin 2018 and Image J-Fiji software were used for data analysis.

19. Ethics statement

Institutional review board approval was obtained from Nanjing Stomatological Hospital Ethics Committee (approval number, 2016NL-016[KS]). All animal experiments and experimental protocols were in accordance with the Animal Care and Use Committee of the Medical School of Nanjing University.

20. Results and discussion

20.1. Characterization of nanoliposomes

Liposomes were fabricated via a typical thin-film spin evaporation process. Empty liposomes were developed as a blank control. The UV–Vis absorption peaks of EVO and ICG encapsulated in liposomes were consistent with free EVO (360 nm and 390 nm) and ICG (736 nm and 784 nm) (Fig. 1A). The fluorescence spectra of EI@Lipo showed that the emission peak was located at 835 nm, which was consistent with the emission peak of ICG@Lipo (Fig. 1B). Thereby, EVO and ICG were successfully loaded in liposomes; furthermore, the fluorescence property of ICG was kept after being encapsulated in nanoliposomes. To compare their optical stability, a UV–Vis–NIR spectrophotometer was used to measure the light absorption of EI@Lipo and ICG under laser irradiation for 2 min and 4 min, respectively. Fig. S4A showed the absorption of ICG

and EI@Lipo after 808 nm laser irradiation for 2 min and 4 min, respectively. It suggested that ICG encapsulated in liposomes exhibited improved photostability; in other words, nanoliposomes could be a protective coat for ICG. In addition, to investigate the stability of nanoliposomes, EI@Lipo was dissolved in physiological saline, PBS, DMEM, F12, and FBS and stored at 4 °C for two weeks. Images were recorded before and after the test (Fig. 1C). The presence of ICG and EVO in the nanoliposomes was confirmed by the variation in the average diameter of the nanoliposomes before and after ICG and EVO encapsulation (Fig. 1D). The average diameter of the EI@Lipo was approximately 120 nm, which was larger than liposomes or ICG@Lipo. Transmission electron microscopic images of EI@Lipo exhibited a core-shell sphere with a size of approximately 130 nm (Fig. 1E and F), which was in accordance with the results of DLS analysis (Fig. 1D). Additionally, the size, the UV–Vis–NIR absorption, and the soluble of EI@Lipo stored in PBS were measured on the 0-day, 7th days and 14th days, which was shown in Fig. S3. The investigations confirmed that EI@Lipo was suitable for long-term storage and displayed good stability in isotonic fluid with tissue fluid.

To calculate the drug loading efficiency, drug release of EI@Lipo, the absorption -dissolution Linear fitting curve of ICG and EVO were firstly conducted (Fig. S2A & Fig. S2D). Then we got the drug loading efficiency of EVO and ICG in the liposomes was 87.49% ± 2.79 and 86.05% ± 2.42, respectively (Fig. S2B & Fig. S2E). In order to simulate the drug release under different physiological and pathological conditions, we conducted this experiment in four pH conditions: pH = 7.4 (normal tissue), pH = 7.06 (original tumor stroma), pH = 6.0 (tumor cell cytoplasm), pH = 4.6 (pH value of lysosomal environment, in which we found the EI@Lipo was mainly located.) And from the results of Fig. S2C and Fig. S2F, we could observe that drug release was pH dependent, and the acidic condition was contributed for drug release. After 72 h in pH = 4.6 PBS buffer, over 90% of EVO and ICG were released from the dialysis bag and into the PBS buffer, and more than 60% of EVO and ICG were delivered in pH = 4.6 PBS buffer. However, less than 20% of EVO and ICG were released in the simulated normal tissue fluid environment. This drug release pattern was a good way of tissue protection. And the acidic environment induction of drug release pattern revealed that EVO and ICG would be delivered in the lysosomes and take effect inside of tumor cells, which was a way to raise the accuracy of treatment and reduce the potential risks of hepatic and cardiac toxicity of EVO.

By chance, we found that many bubbles were produced when EVO@Lipo dropped in hydrogen peroxide-containing DMEM. It is well known that H_2O_2 could relaxedly self-decompose in room temperature and neutral pH environment. EVO as a kind of emprotid could accept the ionized H^+ from hydrogen peroxide, which further promotes the decomposition of hydrogen peroxide for the generation of O_2. Therefore, EVO may show HRP-like properties and generate more ROS in the PDT process. Therefore, we wondered whether evodiamine could catalyze H_2O_2. It was worth noting that H_2O_2 decreased in the solution where EVO and H_2O_2 were together, and the more EVO, the less H_2O_2 surplus, thereby, the more H_2O_2 being decomposed (Fig. 1G). In addition, the decomposing was EVO-concentration dependent. To further investigate whether EVO showed HRP-like properties, we conducted a TMB catalysis reaction in the presence of H_2O_2, TMB, and EVO@Lipo. Natural peroxidase (HRP) can catalyze TMB in the presence of H_2O_2. In addition, this catalytic process produces two colorful products that show a UV absorption peak at 370 nm and 652 nm [44]. To assess the catalytic reaction, only TMB and H_2O_2 were set as control, while the response EVO participated was set as the test group. In the test group, two colorful products were generated, which showed a UV absorption peak at 370 nm and 652 nm, which was in accordance with the manufacturer's directions (Fig. 1H). In addition, over time both color products were increased; however, without EVO, no colorful product was in control. To further investigate the ROS generation of ICG@Lipo and EI@Lipo, SOSG agents were used. As shown in Fig. 1I, the singlet oxygen level was significantly enhanced when EI@Lipo with H_2O_2 compared with
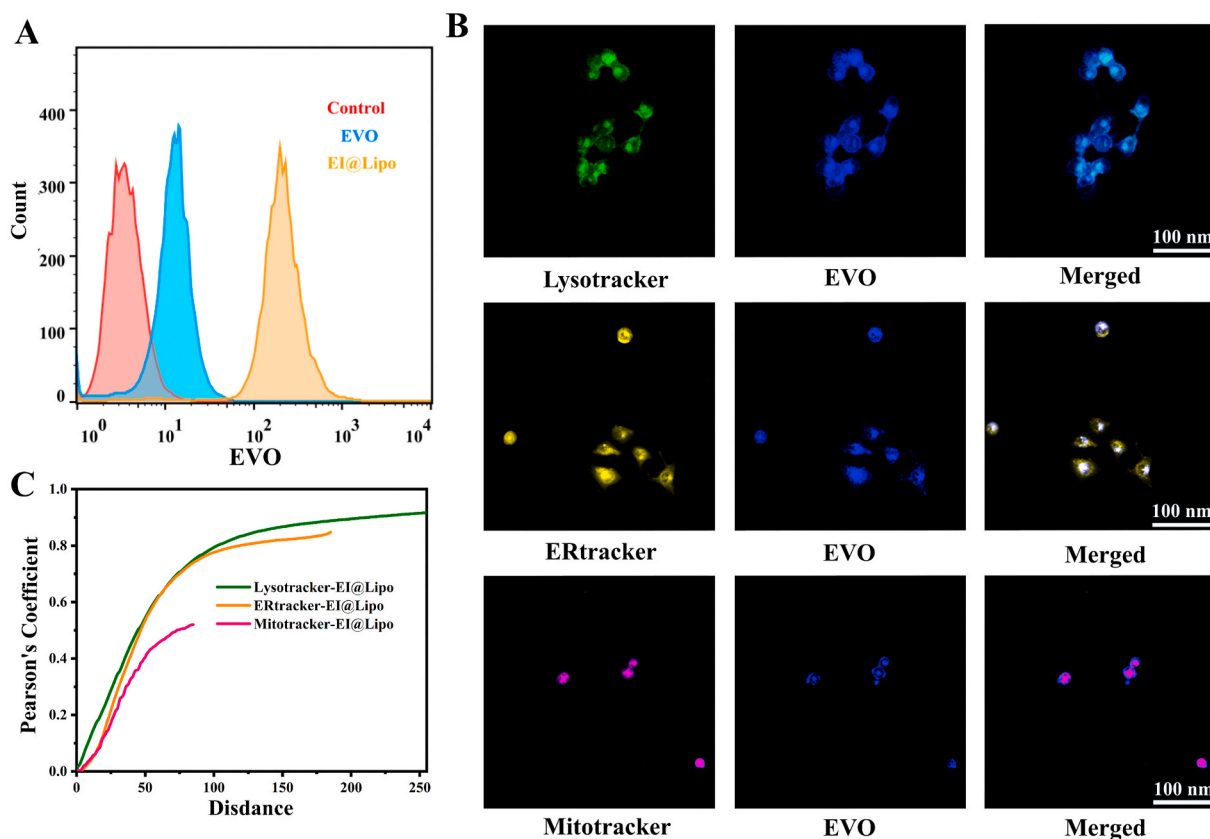
Fig. 2. Intracellular uptake of EVO and EI@Lipo. A. CAL 27 cells were cultured with PBS, EVO, and EI@Lipo overnight. A flow cytometer was used to detect the cellular fluorescence of EVO at 405 nm. The concentration of EVO was 10 μg/mL. Liposomes could notably enhance the cellular uptake of EVO. **B.** Subcellular co-localization between EI@Lipo with Lysosomes, Endoplasmic reticulum and Mitochondria. Scale bar = 100 μm. **C.** Colocalization images of EI@Lipo and LysoTracker, ERtracker and Mitotracker, showed substantial overlap between those channels. Inset: 0.92, 0.89 and 0.53 overlap via Pearson correlation analysis.

ICG@Lipo with H_2O_2. In addition, the EI@Lipo +808 nm laser + H_2O_2 group produced the highest level of singlet oxygen (Fig. S4C). Compared with the ICG@Lipo +808 nm laser group, the singlet oxygen level was much higher in the EI@Lipo +808 nm laser group. In addition, its level was further boosted when H_2O_2 was added to EI@Lipo groups, yet there was no difference in the ICG@Lipo groups. Notably, even without 808 nm laser-excited, the EI@Lipo + H_2O_2 still greatly enhanced the singlet oxygen production (Fig. 1I and Fig. S4C).

Singlet oxygen production was also compared with free ICG. The result was displayed in Fig. S5. We referred to the method of ROS yield calculated using DPBF and methylene blue. To determine the ability of EI@Lipo and to compare the ability between EI@Lipo and free ICG upon 808 nm laser excitation, the fluorescent probe Singlet Oxygen Sensor Green (SOSG) probe was utilized. The intensity of the fluorescence signal at 525 nm is indicative of the amount of singlet oxygen generated. PBS solutions containing SOSG and matched concentrations of either free ICG or EI@Lipo (25 μg/mL) were prepared and irradiated with 808 nm laser (0.5 W). The fluorescence intensity of the solutions at 525 nm was recorded before and 1 min, 2 min, 3 min, 4min, 6 min and 8 min after irradiation. The Singlet oxygen production of ICG was 0.077, and the EI@Lipo revealed significantly enhanced singlet oxygen generation (5.65-fold, Φ $^1O_2$ = 0.44). Consequently, there is evidence to believe that EVO could be an HRP-like substrate to generate ROS and thereby could significantly enhance the ROS levels when EVO and ICG were jointly used, which would boost the antitumor effect.

21. Antitumor efficacy *in vitro*

To examine the intracellular uptake ability of EVO and EI@Lipo, flow cytometry was used after CAL 27, and Fadu cells were incubated

with EVO and EI@Lipo, respectively (Fig. 2A and Fig. S6A). The results showed that liposomes could enhance the intracellular accumulation of EVO. In addition, there was a higher EVO signal in CAL 27 cells than in Fadu cells, indicating that the latter was not as able to uptake the EVO into cells. Besides, the intracellular uptake results of CAL 27 and Fadu cells revealed that nanoliposomes were provided with good drug delivery capability. To further study the intracellular location of EI@Lipo, fluorescence colocalization imaging was used via confocal laser scanning microscopy. CAL 27 cells were pre-incubated with EI@Lipo overnight, and then the lysosomes, endoplasmic reticulum and mitochondria were further stained with typical organelle probe — Lysotracker, ERtracker and Mitotracker, which could specifically label the lysosomes, endoplasmic reticulum, and mitochondria in living cells. As shown in Fig. 2B, with the help of the blue fluorescence signal of EVO, the intracellular localization of EI@Lipo could be easily captured by confocal laser scanning microscopy. The results showed that the blue signal of EVO was largely merged with signals of Lysotracker and ERtracker with Pearson's correlation coefficient of 0.92 and 0.89, respectively, while the Pearson's coefficient between EVO and Mitotracker was only 0.53 (Fig. 2C). The endocytosis of lysosomes contributed for drug releasing.

Since liposomes could deliver more elements into cells, we supposed that the bioavailability of EVO and ICG could be enhanced. We first detected intracellular ROS generation in CAL 27 cells. As it was shown in Fig. 3A, there was significant higher-level ROS signal in cells pre-incubated with EI@Lipo than the ROS level in cells treated with free ICG. There were two possible reasons for this result. On the one hand, liposomes could deliver more ICG into cells; on the other hand, compared with ICG alone, EVO could act as HRP-mimic in lysosomes of cells; thus, much more ROS was generated. To further study the
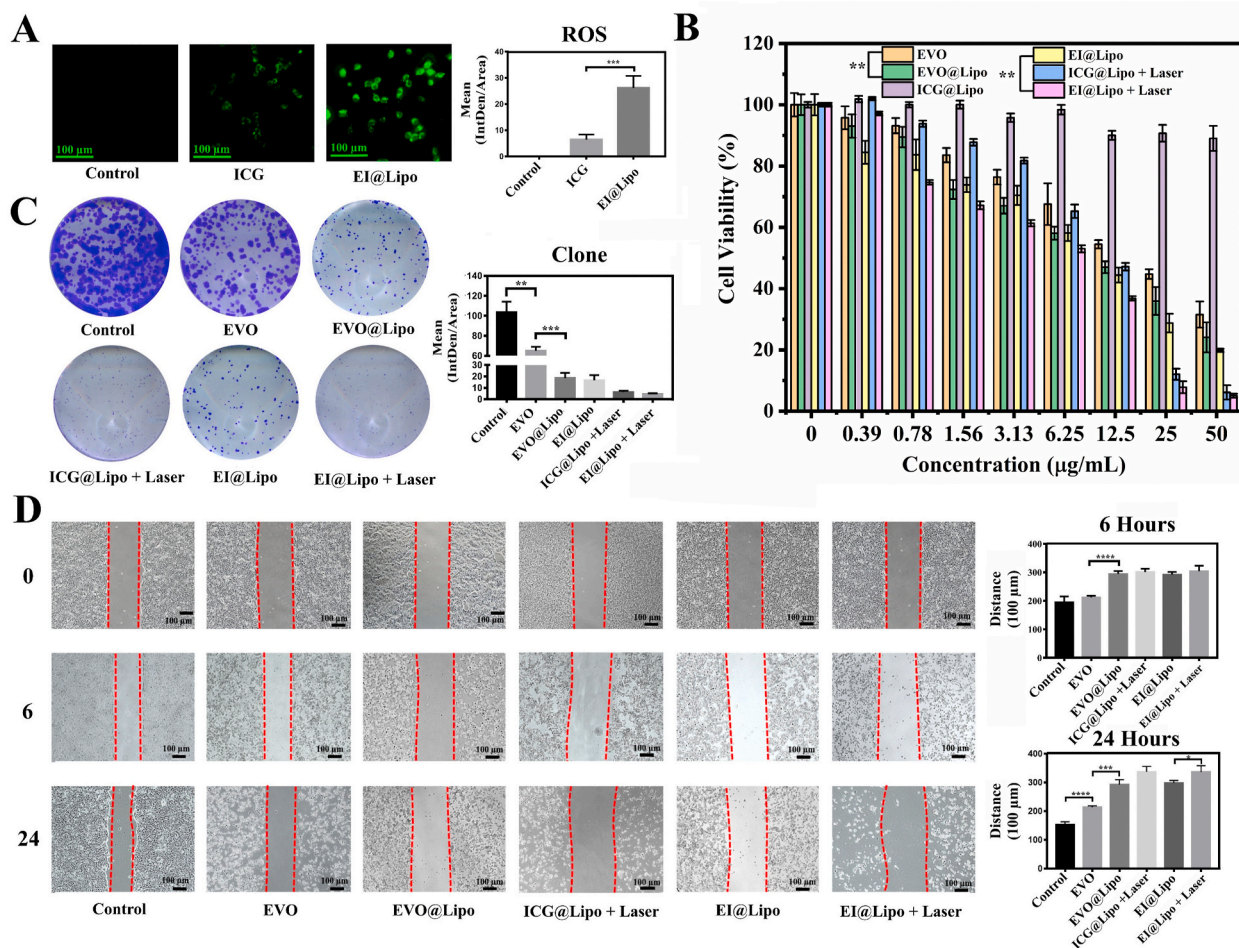
Fig. 3. *In vitro* antitumor efficacy. **A.** Cellular ROS level was signaled by the DCFH-DA probe in green (scale bar = 100 μm). The concentration of EVO and ICG was equaled to 8.07 μg/mL. **B.** The cell proliferation assays were evaluated by CCK-8. CAL 27 cells were treated with various formulations for 24 h. Data was mean ± SD (n = 4). **C.** The clone formation of CAL 27 cells was measured by crystal violet. CAL 2 cells were seeded in a 6-well plate and cocultured with various agents for 24h. **D.** Inhibition migration of CAL 27 cells was examined by wound healing assay after 6 h and 24 h. The experiments were repeated three times. Quantitative analysis was conducted by GraphPad. **: $p < 0.01$; ***: $p < 0.0001$.

Table 1
The IC$_{50}$ values of each group.

The concentrations of EVO or ICG (μg/mL).		
	CAL 27	Fadu
EVO	15.51 ± 1.65	28.85 ± 0.98
EVO@Lipo	9.89 ± 0.20	13.90 ± 0.55
EI@Lipo	9.14 ± 0.87	13.90 ± 0.81
ICG@Lipo + Laser	8.01 ± 0.17	9.56 ± 0.23
EI@Lipo + Laser	5.29 ± 0.66	7.10 ± 0.36

antitumor effect of various nanoliposomes, we then performed cell viability assay using CCK-8. As shown in Fig. 3B and Fig. S6B, the proliferation rates significantly decreased where there existed EVO, which was in a concentration-dependent way. EVO and EVO@Lipo displayed a notable cell inhibition effect. In addition, with the delivery of nanoliposomes, EVO@Lipo and EI@Lipo represented better capability of anti-CAL 27 and Fadu cells compared with EVO-free drugs ($p < 0.01$, $p < 0.001$, respectively). Furthermore, EI@Lipo +808 nm laser did best in inhibiting proliferation, which suggested the combination of chemodynamic, chemical catalysis dynamic, and photodynamic therapy displayed the most potent effect on anticancer cells (Fig. 3B and Fig. S2C). According to the CCK-8 result, IC$_{50}$ values were calculated using Graph prism 7.0, and details were exhibited in Table 1. Compared with the study of GE11-Evo-NPs [33], the combination of EVO and PDT could

significantly reduce the concentration of EVO showing obvious inhibition of cell proliferation, which was a good way for avoiding the potential side effect of EVO. According to the IC$_{50}$, we then selected 10 μg/mL (the average of all IC$_{50}$) for CAL 27 cells and 15 μg/mL (the average of all IC$_{50}$) for Fadu cells of EVO and ICG as the working concentrations for the subsequent experiments. Given the IC$_{50}$ and intracellular uptake results, we considered that Fadu cells might be less sensitive to EVO-related drugs than CAL 27 cells. Cancer cells are known to have a strong ability for proliferation and migration. We then performed the clone formation assay to exam whether EVO containing drugs could inhibit the proliferation and migration of CAL 27 cells and Fadu cells (Fig. 3C and Fig. S6D). The clone formation assay also revealed that the proliferation rates could be significantly decreased when EVO, ICG and 808 nm laser were jointly used. As shown in Fig. 3D, significant migration distance differences could be noticed among control, EVO, EVO@Lipo, ICG@Lipo +808 nm laser, and EI@Lipo +808 nm laser groups, and nanoliposomes containing EVO displayed potent inhibition of CAL 27 cells' migration. Compared with the control group, in EVO containing groups, the number was progressively reduced, and cell morphology was also dramatically changed under the microscope. Therefore, the data *in vitro* suggested the nanoliposome drug delivery system improved the bioavailability of EVO and ICG. In addition, anticancer effect studies demonstrated that the EI@Lipo +808 nm laser (tri-modal therapy of chemodynamic, chemo-, and photodynamic) exhibited the most potent inhibition of anti-proliferation and
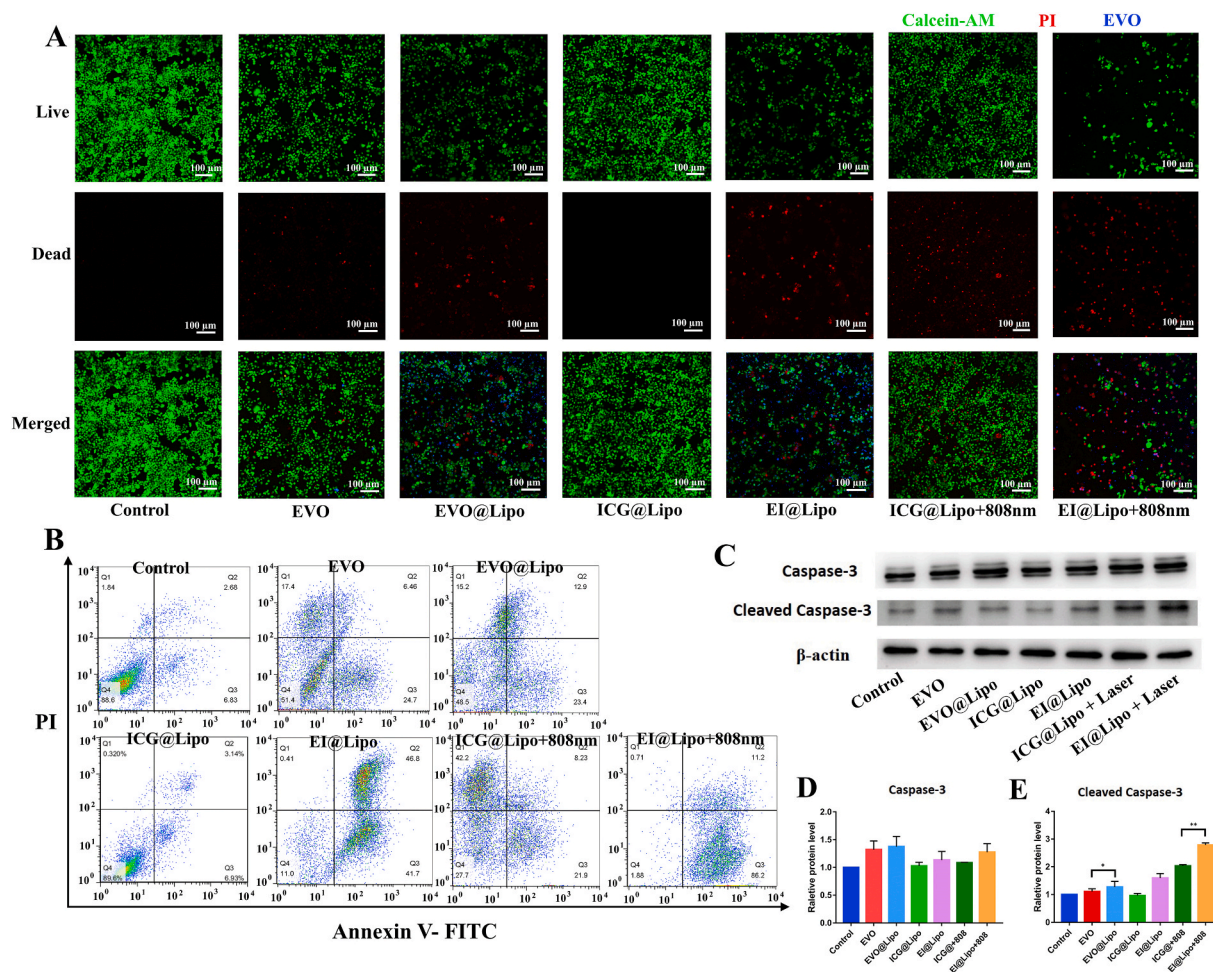
Fig. 4. *In vitro* therapeutic evaluation of EVO, EVO@Lipo, ICG@Lipo, EI@Lipo, ICG@Lipo + 808 nm laser, and EI@Lipo + 808 nm laser. **A.** The fluorescence of Live/Dead cells. Live cells and dead cells were signaled in were signaled in green and red fluorescence, respectively; EVO was shown in blue. Scale bar = 100 μm. **B.** The apoptosis detection of CAL 27 cells analyzed by flow cytometry. Q2: Live cells: Annexin-V$^-$/PI$^-$; Apoptotic cells: Annexin-V$^+$/PI$^-$; Dead cells: Annexin-V$^+$/PI$^+$. **C.** Apoptotic pathway markers of caspase-3 and cleaved caspase-3 were analyzed by Western blot, and the quantitative analysis was shown in D and E. *$p < 0.05$, **$p < 0.01$.

anti-migration, especially for oral squamous carcinoma cells.

22. In vitro chemodynamic therapy evaluation

Reports demonstrated that tri-modal therapy could tremendously inhibit cancer cells. We next investigated the cytotoxic effects of EVO, EVO@Lipo, ICG@Lipo, EI@Lipo, ICG@Lipo +808 nm laser, and EI@Lipo +808 nm laser on the CAL 27 cell line. Live/Dead kit and Apoptosis V-FITC/PI kit were used.

Before loading the Live/Dead cell kit, CAL 27 cells were seeded into a six-well plate and adhered to the wells. Then, cells were pre-incubated with EVO, EVO@Lipo, ICG@Lipo, and EI@Lipo overnight. The result was accessed by the confocal laser microscope. Live cells were stained with Calcein-AM in green fluorescence signal, dead cells were stained with PI in the red signal, and EVO could be detected in blue (Fig. 4A). The cell number was reduced and red dead cells were found in every EVO containing treated group. In addition, in the EI@Lipo +808 nm laser group, the cooperation of EVO based chemical and ICG-based photodynamic effects led to the most considerable reduction in cell number and the largest number of red dead cells. EVO resulted in nearly 70% viable CAL 27 cells, but EVO@Lipo and EI@Lipo led to an increased proportion of early and late-stage apoptotic CAL 27 cells, indicating that it could hardly show its ability in the absence of a drug cargo (Fig. 4B). ICG@Lipo was still with high biocompatibility without 808 nm laser-

excited. Interestingly, the EI@Lipo+808 nm laser resulted in more than 90% apoptotic or dead cells showing that the combined use of chemodynamic, chemical catalysis dynamic and photodynamic effects has great potential in killing cancer cells (Fig. 4A and B). Based on the proliferation of inhibition and cytotoxic effect results, we found that EVO and nanoliposomes containing EVO were more sensitive to CAL 27 cells than Fadu cells (Figs. 3 and 4, and Fig. S6). Cleaved caspase-3 is a well-known key biomarker in the apoptotic pathway. We then detected protein levels via Western blot after the various treatments. As before, EVO containing groups led to the cleaved caspase-3 upregulated expression, and with the nanoliposome cargo, EVO@Lipo and EI@Lipo resulted in more expression of cleaved caspase-3; meanwhile, EI@Lipo +808 nm laser brought about the highest cleaved caspase-3 expression (Fig. 4C–E). Therefore, tri-modal therapy of EI@Lipo +808 nm laser performed effectively antitumor capabilities by inducing apoptosis.

Penetration and accumulation capacity in solid tumor model *in vitro*.

Tumor spheroids are now generally accepted by tumor researchers as a 3D model *in vitro* for anticancer drug screening. Based on the result that EVO displayed a better antitumor effect by packed in a drug cargo, we then studied the nanoliposome delivery and accumulation capability in solid tumor models. We constructed the CAL 27 cell spheroids by suspension culture technology. As shown in Fig. 5A, spheroids could be well-formed using CAL 27 cells, and the diameters of spheroids were approximately 80 μm. Yet, several studies have observed that the tumor
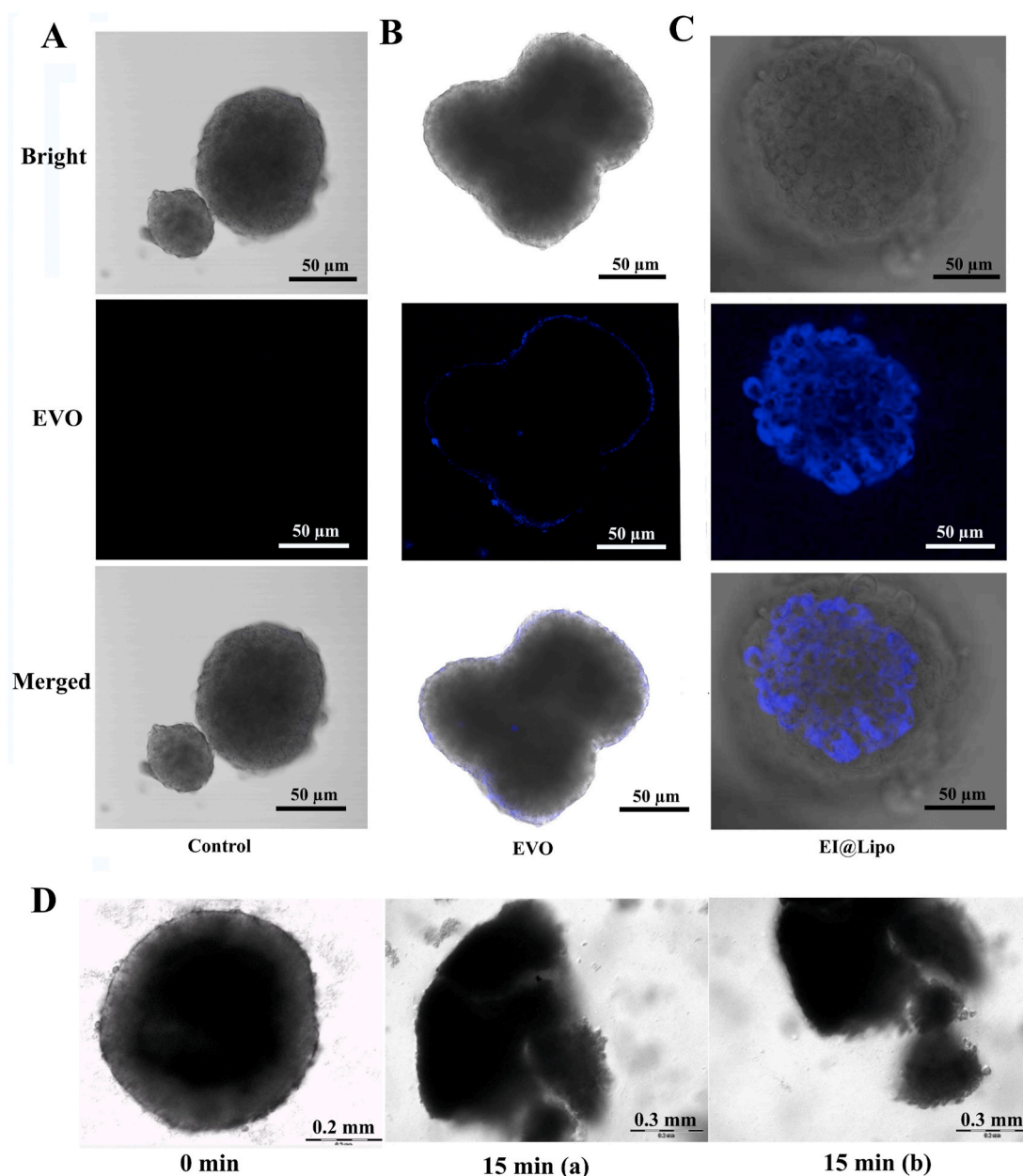
Fig. 5. Penetration and photodynamic therapy in solid tumor spheroid model *in vitro*. Tumor spheroid formation on the 10th day. The diameters were approximately 80 μm. **A–C.** The penetration result of EVO and EI@Lipo after coculturing for 24 h. **B.** EVO only surrounded the edge of the tumor sphere and could not penetrate into the deep. **C.** EI@Lipo penetrated the spheroid and delivered the EVO into cells, which was shown in blue fluorescence. **D.** The CAL 27 sphere was treated with EI@Lipo plus 808 nm laser irradiation at the power of 0.5 W for 15min. The CAL 27 sphere was defeated into pieces after 15 min irradiation. The pictures were screenshots from the therapy process video 2 and 3.

size has effects on tumor curability using various photodynamic and chemotherapy treatments [45,46]. Besides, hypoxia and nutrient depletion, for instance, would occur in non-vascularized tissue at diameters greater than 100 μm [47]. Therefore, we tested the nanoliposomes' penetration and drug accumulation capability when the diameter of the tumor spheroids reached more than 500 μm on the 15th day. Due to CAL 27 cells were more sensitive to EVO, CAL 27 spheroids were selected for the following experiments. CAL 27 spheroids were cocultured with EVO and EI@Lipo for 24 h. We first detected the accumulation of EVO and EI@Lipo under the confocal microscope. Compared with the EVO-treated group, EI@Lipo accumulated almost the whole spheroid with full of blue fluorescence (Fig. 5C), whereas the EVO treated spheroid only with blue fluorescence surrounding the edge (Fig. 5B). In the meantime, we also scanned and recorded the

fluorescence of different layers of the sphere, which could be seen in Video 1. The result of Fig. 5C and Video 1 indicated that EI@Lipo could penetrate the inside of the tumor spheroid and then deliver the EVO drug to cells. However, EVO had poor penetration ability. Besides, the live cell station was to be used to monitor the process of EI@Lipo's penetration (Video 2). We found that EI@Lipo slowly accumulated into the CAL 27 sphere, and its edge differed from it as before. Photodynamic therapy and ROS production could be affected in the hypoxia microenvironment. Therefore, we detected the photodynamic effect in the tumor model (Fig. 5D). The process was also recorded by the live cell station in the Video 3. The CAL 27 spheroid was defeated into pieces after the 808 nm laser irradiation at the power of 0.5 W for 15 min (Fig. 5D). Consequently, the EI@Lipo could penetrate deeply into the tumor spheroid. In the tumor model, the photodynamic effect of
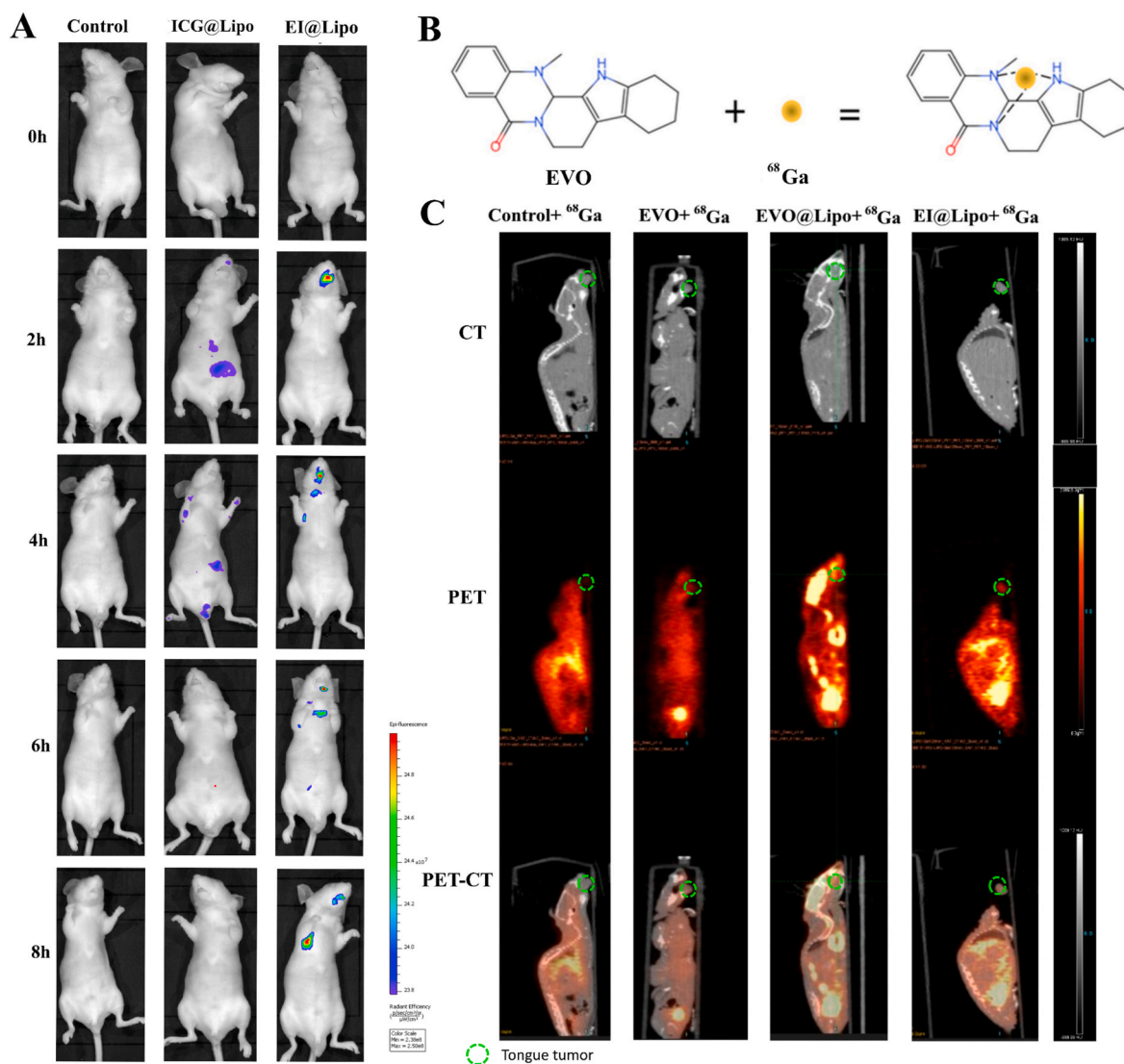
Fig. 6. Bimodal live imaging of EI@Lipo on the tumor-bearing murine model of tongue cancer in situ. A. 808 nm excitation fluorescence images of control, ICG, and EI@Lipo. Pictures were obtained every 2 h after the tail injection. **B.** The reaction between EVO and ^{68}Ga. **C.** The PET-CT images of control+^{68}Ga, EVO+^{68}Ga, EVO@Lipo+^{68}Ga, and EI@Lipo+^{68}Ga. In addition, pictures were obtained after 0.5 h of tail injection. The tongue tumor was signaled in a green circle.

EI@Lipo could still hold great power of energy for anticancer, even when the diameter of the tumor 3D model reached more than 500 μm, where there tended to be in a hypoxia environment. Bimodal live imaging of EI@Lipo on tumor-bearing mice model of tongue cancer in situ.

Supplementary video related to this article can be found at doi:10.1016/j.bioactmat.2020.12.016

Encouraged by the superior anticancer efficacy and drug delivery capacity of EI@Lipo via the tri-modal therapy way under 808 nm laser *in vitro*, we then conducted animal experiments to confirm our hypothesis that the combination of EVO based chemo/chemodynamic and ICG-based photodynamic therapy could have a significant effect on anticancer *in vivo*. To evaluate the anticancer efficacy, tongue cancer in situ imaging and biodistribution of free ICG and EI@Lipo were first detected. It was observed that ICG and EI@Lipo exhibited comparable ICG accumulation in the tumor site at either 2 h, 4 h, 6 h, or 8 h post tail injection (Fig. 6A) via Xenogen IVIS® Lumia machine. After the tongue cancer mice were sacrificed, the fluorescence intensity in different organs from free ICG and EI@Lipo groups was measured. As shown in Fig. 6A, EI@Lipo treated mice exhibited significantly enhanced fluorescence signals in the tumor tissue from 2 h to 8 h post-injection compared with free ICG. In addition, the quantitative results demonstrated that

EI@Lipo exhibited a 1.833-fold higher fluorescence signal at tumor sites 10 h post-injection (Fig. S7). Therefore, compared with free ICG, nanoliposomes remarkably enhanced the accumulation level in tumors and prolonged the circulation time *in vivo*. Besides, a similar result could be observed that the aggregation location of ICG was similar, but EI@Lipo could deliver more ICG in the tumor site and stay longer. It is vital to precisely focus the laser beam on the tumor area to release EVO during the PDT process to enhance the anticancer efficacy and finally realize the trimodal therapy. Yet, precise tumor focusing relied on precise tumor imaging. In addition, due to the chelated structure between EVO and ^{68}Ga, we finally got two means for tongue tumor imaging; one was the fluorescence imaging (FI), and the other was PET-CT (Fig. 6A and C). Given the FI and PET-CT bi-model imaging, we then located the cancer at the tip of the tongue, which agrees with the inoculation area. As far as we knew, there have been very few experiments to image tongue carcinoma in situ and many NPs probes was applied on transplanted tumor model [7,34], probably because the tongue tumor was too small to locate and the success rate of establishing the tongue tumor in situ was low. However, with the delivery of liposome and the chelation of EVO with ^{68}Ga, we could see the tumor outline and located the tiny tumor at the tip of the tongue.
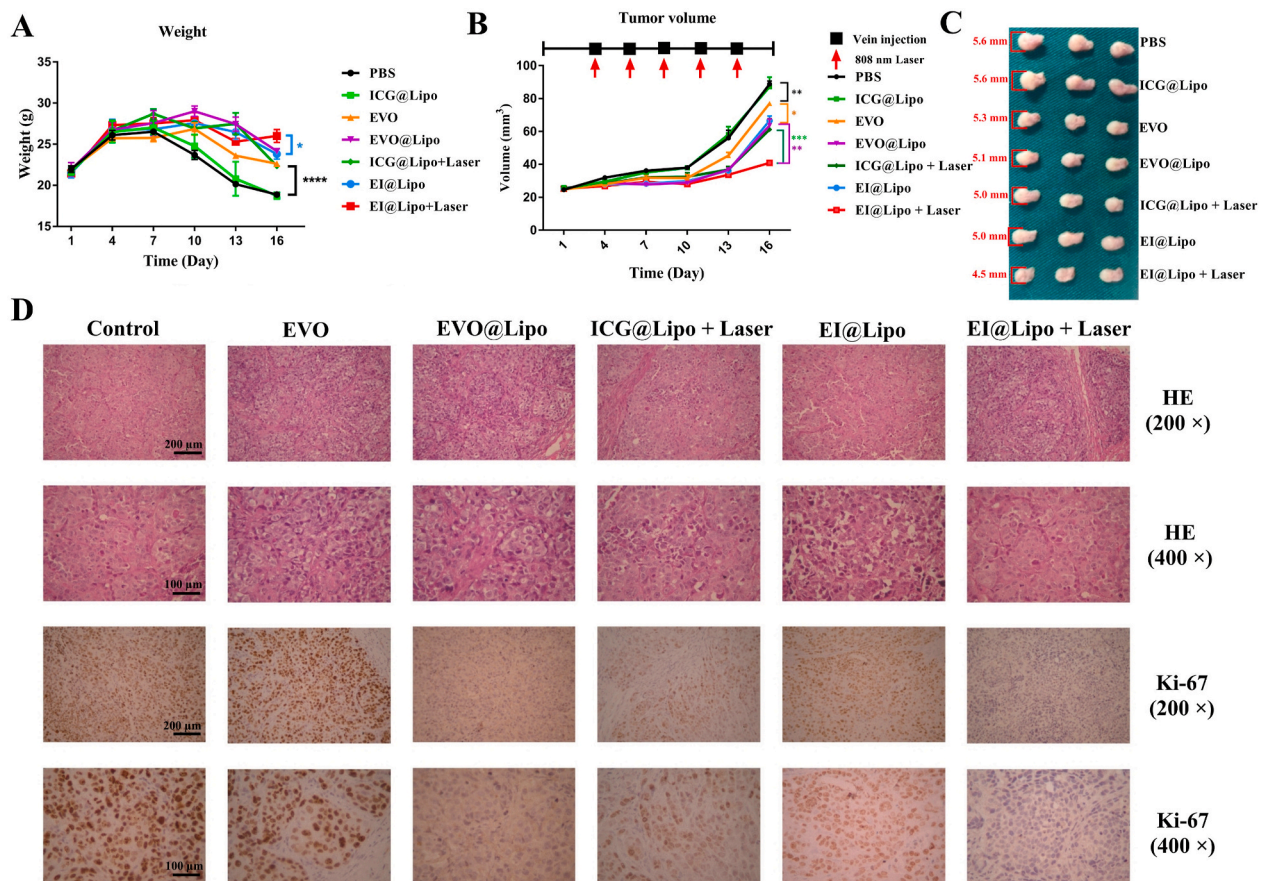
Fig. 7. Tri-modal therapy against Tongue Squamous Cell Carcinoma *in vivo*. After the tumor volume reached 20 mm^3, the therapies were performed every three days with the equivalent EVO dose of 2.0 mg/kg or an ICG dose of 2.0 mg/kg. **A.** The body weight was monitored before the injections. The body weight loss with the tongue tumor growth in the PBS and ICG@Lipo groups. However, mice treated with EI@Lipo +808 nm showed the weight rise again. **B.** Tumor growth profiles of CAL 27 tongue tumor xenograft-bearing nude mice via different treatments. * <0.5, ** <0.01, *** <0.001. **C.** Representative CAL 27 tongue tumors picture at the end of treatments. **D.** The immunohistochemical studies (H&E and Ki-67) of tongue cancer slices. The brown staining of the nucleus indicated the positive expression of Ki-67, and the higher the positive rate, the stronger proliferation of tumor cells.

Chemo/chemodynamic/photodynamic tri-modal therapy against tongue squamous cell carcinoma and biocompatibility evaluation *in vivo*.

Under the guidance of FI and PET-CT bimodal imaging, the *in vivo* anticancer efficacy of EI@Lipo under 808 nm laser irradiation was subsequently conducted on CAL 27 tongue tumor-bearing mice. A total of 21 tumor-bearing mice were randomly divided into seven groups (n = 3): PBS, ICG@Lipo, EVO, EVO@Lipo, EI@Lipo, ICG@Lipo + 808 nm laser, and EI@Lipo + 808 nm laser. When the tumor volume reached 20, treatments were started. Mice were administered via the tail vein with a dose of 2 mg EVO or ICG kg^{-1}, and administrations were conducted every three days. Since the highest level of tumor FI signal was 2 h post-injection, the tumor tissue was precisely irradiated with 808 nm laser 2 h after injection. The mice weights and tumor sizes were monitored over the following 16 days. In addition, then tumor volume was followed by the formula. With the increase in tumor volume, swallowing and eating became more difficult, and the weight of mice gradually decreased (Fig. 7A), especially in PBS and ICG@Lipo treated groups, except the mice treated with EI@Lipo + 808 nm laser, and in this group the weight of mice showed an upward trend. As shown in Fig. 7B, treatment with free EVO showed tumor growth inhibition compared with PBS treatment mice (*p* = 0.031). In contrast, treatments with EVO@Lipo and EI@Lipo induced significant tumor growth inhibition, which was due to enhanced EVO accumulation in the tumor with the delivery of nano-liposomes. Having established that ICG@Lipo and EI@Lipo could produce ROS excited with 808 nm laser irradiation and that the

combination of EVO and ICG exhibited great anticancer power *in vitro*, their abilities to produce NIR-triggered ROS were also investigated *in vivo*. As expected, in the ICG@Lipo +808 nm laser group, there was inhibition of tumor growth. In contrast, the EI@Lipo +808 nm laser group displayed the highest inhibition efficacy for tumor growth (*p* < 0.001), which indicated that the EVO release during the ICG-based PDT process could significantly induce the cascade-amplifying synergistic effects of chemo-photodynamic therapy. In addition, the boosted EVO released from EI@Lipo was capable of triggering cascade-like chemotherapy to continuously destroy the remaining tumor cells after PDT, thus achieving the synergistic therapeutic effects of chemo-photodynamic therapy with great antitumor power. The observed results in tumor growth were further confirmed by tumor weight and representative tumor images (Fig. 7C). Furthermore, the immunohistochemical studies (H&E and Ki-67) of tongue cancer slices also highly supported the antitumor efficacy post various therapies (Fig. 7D). The highest cell proliferation was observed in PBS treated mice (Ki-67 positive >90%). In contrast, few Ki-67 positive cells were observed in tumor slices treated with EI@Lipo +808 nm (Ki-67 positive <10%), which revealed the lowest level of tumor cell proliferation. Therefore, the tri-modal theranostic EI@Lipo held superior anticancer efficacy and drug delivery capacity.

23. Biocompatibility evaluation in SD rats

For the potential biomedical application, the biotoxicity of drugs is a
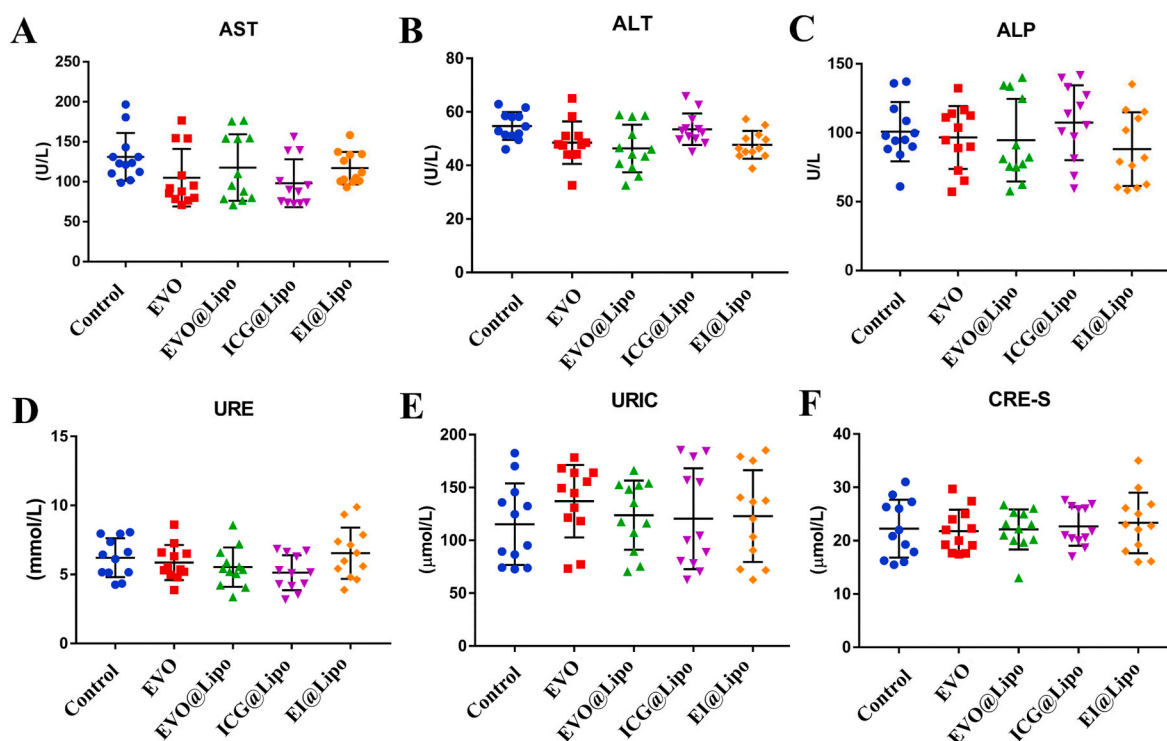
Fig. 8. Biosafety assessment of different agents. The liver and kidney function detection of SD rats fed with PBS, EVO, EVO@Lipo, ICG@Lipo, and EI@Lipo. The dose of EVO and ICG was 2.0 mg/kg. **A–C** showed the liver function detection. **D–F** showed the kidney function detection. There were no significant differences between groups.

primary concern. The biocompatibility of various nano liposome-based drugs was conducted. SD rats were administered PBS, EVO, EVO@-Lipo, ICG@Lipo, and EI@Lipo for 60 days, and the dose of EVO and ICG was 2.0 mg/kg. Blood samples were obtained from the tails of SD rats every five days. All SD rats were fed for 60 days. Given the H&E-stained results, they caused no noticeable pathological changes to major organs (heart, liver, spleen, lung, and kidney) (Fig. S8). Besides, the results of liver function and renal function indexes of SD rats showed no differences among all treated groups, suggesting that the drugs used did not harm the function of the liver and kidney (Fig. 8). These results indicated that all of the tested agnostic liposome drugs were bio-safe to SD rats' main organs. In contrast, the EI@Lipo based chemo/chemo-dynamic/photodynamic tri-modal therapy displayed an extraordinary capability against tongue squamous cell carcinoma.

24. Conclusions

In summary, we successfully developed a Chinese medicine-EVO based novel nanoliposome with precise FI and PET-CT imaging-guided chemo/chemodynamic/photodynamic tri-modal therapy against tongue squamous cell carcinoma. The co-assembled nanoliposomes are characterized by high and stable drug loading properties, superior stability, and significant anticancer activity *in vitro*. Notably, we were surprised to find that Chinese medicine EVO has not only anticancer efficacy but also shows enhanced sensitivity to tongue squamous cell carcinoma cells. Additionally, to our knowledge, it is the first time EVO was used for anti-tongue cancer and that the HRP-like catalysis of EVO was explored to generate ROS. The core-shell structure nanoliposomes loaded with EVO and ICG could deeply penetrate the tumor and possessed significant power for inhibiting cancer cell proliferation and finally induce cancer cell apoptosis both *in vitro* and *in vivo*. The disassembled nanoliposomes subsequently enhanced EVO release during the 808 nm laser-induced ICG PDT process, thus triggering a chemo cascaded therapy to annihilate the remaining cancer cells together with the PDT synergistically.

Furthermore, the nano EI@Lipo could precisely locate the small tongue tumor via FI and PET-CT bi-modal imaging, and the nanoliposomes could boost the EVO accumulation in the tumor, prolonging its retention time. At the same time, the EI@Lipo showed superior biosafety without harming healthy organs. Overall, the nano EI@Lipo is essentially a nano-biomaterial agent with dual imaging and tri-modal therapy properties for anticancer. In addition, our study provided a promising approach for releasing cascade-amplifying effects of chemo-photodynamic treatment, and it is of great benefit to expand the application of traditional Chinese medicine.

CRediT authorship contribution statement

Zheng Wei: Conceptualization, Investigation, Writing - original draft, Methodology, Software, Funding acquisition. **Huihui Zou:** Conceptualization, Investigation, Writing - original draft, Methodology, Software, Funding acquisition. **Gongyuan Liu:** Investigation, Data curation, Writing - original draft. **Chuanhui Song:** Investigation, Data curation, Writing - original draft. **Chuanchao Tang:** Investigation, Data curation, Writing - original draft. **Sheng Chen:** Visualization, Investigation. **Guorong Zhang:** Visualization, Investigation. **Jianchuan Ran:** Visualization, Investigation. **Yufeng Wang:** Visualization, Investigation. **Yu Cai:** Supervision, Validation, Formal analysis, Writing - review & editing, Funding acquisition. **Wei Han:** Supervision, Validation, Formal analysis, Writing - review & editing, Funding acquisition.

Declaration of competing interest

The authors declare that they have no known competing financial interests or personal relationships that could have appeared to influence the work reported in this paper.

Acknowledgments

Appendix A. Supplementary data

Supplementary data to this article can be found online at https://doi.org/10.1016/j.bioactmat.2020.12.016.

The IC_{50} value of EI@Lipo was the concentration of EVO.

References

[1] F. Bray, J. Ferlay, I. Soerjomataram, R.L. Siegel, L.A. Torre, A. Jemal, Global cancer statistics 2018: GLOBOCAN estimates of incidence and mortality worldwide for 36 cancers in 185 countries, CA A Cancer J. Clin. 68 (6) (2018) 394–424.

[2] P.J. Thomson, Perspectives on oral squamous cell carcinoma prevention-proliferation, position, progression and prediction, J. Oral Pathol. Med. 47 (9) (2018) 803–807.

[3] X.H. Yang, X.X. Zhang, Y. Jing, L. Ding, Y. Fu, S. Wang, S.Q. Hu, L. Zhang, X.F. Huang, Y.H. Ni, Q.G. Hu, Amino acids signatures of distance-related surgical margins of oral squamous cell carcinoma, EBioMedicine 48 (2019) 81–91.

[4] T.C. Chen, H.L. Chang, T.L. Yang, P.J. Lou, Y.L. Chang, J.Y. Ko, C.P. Wang, Impact of dysplastic surgical margins for patients with oral squamous cell carcinoma, Oral Oncol. 97 (2019) 1–6.

[5] C.R. Anderson, K. Sisson, M. Moncrieff, A meta-analysis of margin size and local recurrence in oral squamous cell carcinoma, Oral Oncol. 51 (5) (2015) 464–469.

[6] M. Kamat, B.D. Rai, R.S. Puranik, U.V. Datar, A comprehensive review of surgical margin in oral squamous cell carcinoma highlighting the significance of tumor-free surgical margins, J. Canc. Res. Therapeut. 15 (3) (2019) 449–454.

[7] N. Patel, P. Pera, P. Joshi, M. Dukh, W.A. Tabaczynski, K.E. Siters, M. Kryman, R.R. Cheruku, F. Durrani, J.R. Missert, R. Watson, T.Y. Ohulchanskyy, E.C. Tracy, H. Baumann, R.K. Pandey, Highly effective dual-function near-infrared (NIR) photosensitizer for fluorescence imaging and photodynamic therapy (PDT) of cancer, J. Med. Chem. 59 (21) (2016) 9774–9787.

[8] E.A. Owens, M. Henary, G. El Fakhri, H.S. Choi, Tissue-specific near-infrared fluorescence imaging, Acc. Chem. Res. 49 (9) (2016) 1731–1740.

[9] Y. Li, Y. Sun, J. Li, Q. Su, W. Yuan, Y. Dai, C. Han, Q. Wang, W. Feng, F. Li, Ultrasensitive near-infrared fluorescence-enhanced probe for in vivo nitroreductase imaging, J. Am. Chem. Soc. 137 (19) (2015) 6407–6416.

[10] F. An, N. Chen, W.J. Conlon, J.S. Hachey, J. Xin, O. Aras, E.A. Rodriguez, R. Ting, Small ultra-red fluorescent protein nanoparticles as exogenous probes for noninvasive tumor imaging in vivo, Int. J. Biol. Macromol. 153 (2020) 100–106.

[11] A.L. Vahrmeijer, M. Hutteman, J.R. van der Vorst, C.J. van de Velde, J.V. Frangioni, Image-guided cancer surgery using near-infrared fluorescence, Nat. Rev. Clin. Oncol. 10 (9) (2013) 507–518.

[12] M. Saccomano, C. Dullin, F. Alves, J. Napp, Preclinical evaluation of near-infrared (NIR) fluorescently labeled cetuximab as a potential tool for fluorescence-guided surgery, Int. J. Canc. 139 (10) (2016) 2277–2289.

[13] N. Zaidi, E. Bucak, A. Okoh, P. Yazici, H. Yigitbas, E. Berber, The utility of indocyanine green near infrared fluorescent imaging in the identification of parathyroid glands during surgery for primary hyperparathyroidism, J. Surg. Oncol. 113 (7) (2016) 771–774.

[14] Y. Wang, D. Xie, Z. Wang, X. Zhang, Q. Zhang, Y. Wang, A.D. Newton, S. Singhal, H. Cai, Y. Wang, Q. Lu, Q. Hu, Z. Wang, Kinetics of indocyanine green: optimizing tumor to normal tissue fluorescence in image-guided oral cancer surgery applications, Head Neck 41 (4) (2019) 1032–1038.

[15] J. Hu, Y. Tang, A.H. Elmenoufy, H. Xu, Z. Cheng, X. Yang, Nanocomposite-based photodynamic therapy strategies for deep tumor treatment, Small 11 (44) (2015) 5860–5887.

[16] Y. Wang, D. Xie, J. Pan, C. Xia, L. Fan, Y. Pu, Q. Zhang, Y.H. Ni, J. Wang, Q. Hu, A near infrared light-triggered human serum albumin drug delivery system with coordination bonding of indocyanine green and cisplatin for targeting photochemistry therapy against oral squamous cell cancer, Biomater Sci 7 (12) (2019) 5270–5282.

[17] S. Ren, X. Cheng, M. Chen, C. Liu, P. Zhao, W. Huang, J. He, Z. Zhou, L. Miao, Hypotoxic and rapidly metabolic PEG-PCL-C3-ICG nanoparticles for fluorescence-guided photothermal/photodynamic therapy against OSCC, ACS Appl. Mater. Interfaces 9 (37) (2017) 31509–31518.

[18] E.P. Gusti-Ngurah-Putu, L. Huang, Y.C. Hsu, Effective combined photodynamic therapy with lipid platinum chloride nanoparticles therapies of oral squamous carcinoma tumor inhibition, J. Clin. Med. 8 (12) (2019).

[19] L. Larue, B. Myrzakhmetov, A. Ben-Mihoub, A. Moussaron, N. Thomas, P. Arnoux, F. Baros, R. Vanderesse, S. Acherar, C. Frochot, Fighting hypoxia to improve PDT, Pharmaceuticals 12 (4) (2019).

[20] X. Li, N. Kwon, T. Guo, Z. Liu, J. Yoon, Innovative strategies for hypoxic-tumor photodynamic therapy, Angew Chem. Int. Ed. Engl. 57 (36) (2018) 11522–11531.

[21] J.G. Yang, R. Lu, X.J. Ye, J. Zhang, Y.Q. Tan, G. Zhou, Icaritin reduces oral squamous cell carcinoma progression via the inhibition of STAT3 signaling, Int. J. Mol. Sci. 18 (1) (2017).

[22] T. Wu, H. Cui, Y. Xu, Q. Du, E. Zhao, J. Cao, L. Nie, G. Fu, A. Ren, The effect of tubeimoside-1 on the proliferation, metastasis and apoptosis of oral squamous cell carcinoma in vitro, OncoTargets Ther. 11 (2018) 3989–4000.

[23] Q. Tan, J. Zhang, Evodiamine and its role in chronic diseases, Adv. Exp. Med. Biol. 929 (2016) 315–328.

[24] Y.X. Xuechao Lu, QIhua Xie, Clinical study on the treatment of diabetic gastroparesis with hot compress of Fructus evodiae and ginger juice, Journal of Practical Diabetes 16 (2020) 56–57.

[25] Y.J. Xiong, D.P. Chen, J.Y. Peng, J.Y. Wang, B.C. Lv, F.F. Liu, Y. Lin, Characteristics of evodiamine-exerted stimulatory effects on rat jejunal contractility, Nat. Prod. Res. 29 (4) (2015) 388–391.

[26] J. Wei, Z. Li, F. Yuan, Evodiamine might inhibit TGF-beta1-induced epithelial-mesenchymal transition in NRK52E cells via Smad and PPAR-gamma pathway, Cell Biol. Int. 38 (7) (2014) 875–880.

[27] Y.W. Shin, E.A. Bae, X.F. Cai, J.J. Lee, D.H. Kim, In vitro and in vivo antiallergic effect of the fructus of Evodia rutaecarpa and its constituents, Biol. Pharm. Bull. 30 (1) (2007) 197–199.

[28] J. Jiang, C. Hu, Evodiamine: a novel anti-cancer alkaloid from Evodia rutaecarpa, Molecules 14 (5) (2009) 1852–1859.

[29] K. Sachita, Y. Kim, H.J. Yu, S.D. Cho, J.S. Lee, Vitro assessment of the anticancer potential of evodiamine in human oral cancer cell lines, Phytother Res. 29 (8) (2015) 1145–1151.

[30] Q. Guo, Y. Liu, J. Zhao, J. Wang, Y. Li, Y. Pang, J. Chen, J. Wang, Evodiamine inactivates NF-kappaB and potentiates the antitumor effects of gemcitabine on tongue cancer both in vitro and in vivo, OncoTargets Ther. 12 (2019) 257–267.

[31] H.X. Jiahao Mo, Li Jing, Jinsheng Li, Xiangjun Qi, Chong Zhong, Discussion on mechanism of *Zuojin* pills in treatment of hepatocellular carcinoma based on network pharmacology, Chinese Journal of traditional Chinese medicine information 28 (2020) 1–9.

[32] Q. Sun, L. Xie, J. Song, X. Li, Evodiamine: a review of its pharmacology, toxicity, pharmacokinetics and preparation researches, J. Ethnopharmacol. 262 (2020), 113164.

[33] C. Li, G. Cai, D. Song, R. Gao, P. Teng, L. Zhou, Q. Ji, H. Sui, J. Cai, Q. Li, Y. Wang, Development of EGFR-targeted evodiamine nanoparticles for the treatment of colorectal cancer, Biomater Sci 7 (9) (2019) 3627–3639.

[34] S. Chen, G. Dong, S. Wu, N. Liu, W. Zhang, C. Sheng, Novel fluorescent probes of 10-hydroxyevodiamine: autophagy and apoptosis-inducing anticancer mechanisms, Acta Pharm. Sin. B 9 (1) (2019) 144–156.

[35] S. Gao, G. Tang, D. Hua, R. Xiong, J. Han, S. Jiang, Q. Zhang, C. Huang, Stimuli-responsive bio-based polymeric systems and their applications, J. Mater. Chem. B 7 (5) (2019) 709–729.

[36] W. Ma, Y. Ding, M. Zhang, S. Gao, Y. Li, C. Huang, G. Fu, Nature-inspired chemistry toward hierarchical superhydrophobic, antibacterial and biocompatible nanofibrous membranes for effective UV-shielding, self-cleaning and oil-water separation, J. Hazard Mater. 384 (2020) 121476.

[37] Y. Ruan, X. Jia, C. Wang, W. Zhen, X. Jiang, Mn-Fe layered double hydroxide nanosheets: a new photothermal nanocarrier for O2-evolving phototherapy, Chem. Commun. 54 (83) (2018) 11729–11732.

[38] Z. Tang, Y. Liu, M. He, W. Bu, Chemodynamic therapy: tumour microenvironment-mediated Fenton and fenton-like reactions, Angew Chem. Int. Ed. Engl. 58 (4) (2019) 946–956.

[39] L.S. Lin, J. Song, L. Song, K. Ke, Y. Liu, Z. Zhou, Z. Shen, J. Li, Z. Yang, W. Tang, G. Niu, H.H. Yang, X. Chen, Simultaneous fenton-like ion delivery and glutathione depletion by MnO2 -based nanoagent to enhance chemodynamic therapy, Angew Chem. Int. Ed. Engl. 57 (18) (2018) 4902–4906.

[40] H. Liu, Y. Hu, Y. Sun, C. Wan, Z. Zhang, X. Dai, Z. Lin, Q. He, Z. Yang, P. Huang, Y. Xiong, J. Cao, X. Chen, Q. Chen, J.F. Lovell, Z. Xu, H. Jin, K. Yang, Co-delivery of bee venom melittin and a photosensitizer with an organic-inorganic hybrid nanocarrier for photodynamic therapy and immunotherapy, ACS Nano 13 (11) (2019) 12638–12652.

[41] J. Atchison, S. Kamila, H. Nesbitt, K.A. Logan, D.M. Nicholas, C. Fowley, J. Davis, B. Callan, A.P. McHale, J.F. Callan, Iodinated cyanine dyes: a new class of sensitisers for use in NIR activated photodynamic therapy (PDT), Chem. Commun. 53 (12) (2017) 2009–2012.

[42] Y. Cheng, A.C. Samia, J.D. Meyers, I. Panagopoulos, B. Fei, C. Burda, Highly efficient drug delivery with gold nanoparticle vectors for in vivo photodynamic therapy of cancer, J. Am. Chem. Soc. 130 (32) (2008) 10643–10647.

[43] S. Ji, A. Czerwinski, Y. Zhou, G. Shao, F. Valenzuela, P. Sowinski, S. Chauhan, M. Pennington, S. Liu, (99m)Tc-Galacto-RGD2: a novel 99mTc-labeled cyclic RGD peptide dimer useful for tumor imaging, Mol. Pharm. 10 (9) (2013) 3304-3314.

[44] X. Jiang, C. Sun, Y. Guo, G. Nie, L. Xu, Corrigendum to "Peroxidase-like activity of apoferritin paired gold clusters for glucose detection, Biosens. Bioelectron. 64 (2015) 165–170. Biosens Bioelectron 94 (2017) 731.

[45] E.C. Costa, A.F. Moreira, D. de Melo-Diogo, V.M. Gaspar, M.P. Carvalho, I. J. Correia, 3D tumor spheroids: an overview on the tools and techniques used for their analysis, Biotechnol. Adv. 34 (8) (2016) 1427–1441.

[46] A.S. Nunes, A.S. Barros, E.C. Costa, A.F. Moreira, I.J. Correia, 3D tumor spheroids as in vitro models to mimic in vivo human solid tumors resistance to therapeutic drugs, Biotechnol. Bioeng. 116 (1) (2019) 206–226.

[47] M. Hockel, P. Vaupel, Tumor hypoxia: definitions and current clinical, biologic, and molecular aspects, J. Natl. Cancer Inst. 93 (4) (2001) 266–276.